Influence of the transient airflow pattern on the temporal evolution of microparticle resuspension: Application to ventilated duct during fan acceleration

Félicie Theron, Djihad Debba, Laurence Le Coq

Version auteur acceptée dans Aerosol Science and Technology
https://doi.org/10.1080/02786826.2022.2120793

Influence of the transient airflow pattern on the temporal evolution of microparticle resuspension: Application to ventilated duct during fan acceleration

Félicie Theron, Djihad Debba, and Laurence Le Coq

IMT Atlantique, CNRS, GEPEA, UMR 6144, Nantes, France

ABSTRACT

This study investigates experimentally the influence of the temporal airflow pattern properties to which microparticles are exposed on the dynamics of the resuspension phenomenon for transient airflow conditions representative of a fan start, i.e., involving a temporal acceleration period before reaching steady state. The extent to which the average steady state velocity and the average acceleration affect the characteristics of the curve depicting the temporal evolution of the fraction of particles remaining on the duct wall, i.e., the time at which resuspension starts and the curve shape, is investigated. These results are analyzed regarding the properties of the instantaneous velocity signal in the viscous sublayer. It is demonstrated that a threshold turbulent kinetic energy must be exceeded for resuspension to begin. The results are also presented in terms of resuspension rate, i.e., of instantaneous rate of particles removed from the duct surface, versus time. This enables to demonstrate that the highest resuspension rate values are recorded at the very beginning of the phenomenon, typically during the fan acceleration stage, and that high mean acceleration values are responsible for high resuspension rates.

1. Introduction

The resuspension phenomenon consists in the detachment of microparticles from a surface. Depending on the considered situation one may wish to limit or in contrast to promote resuspension. For applications such as management of air treatment facilities dedicated to indoor air blowing in working or manufacturing areas, resuspension of microparticles can represent either contamination or damage risks regarding products, or sanitary risks toward populations. As mentioned by Liu et al. (2020), the understanding of particle resuspension mechanisms in Heating Ventilating and Air Conditioning (HVAC) ducts is essential to control the biological contamination of indoor air by fungal spores for example. Conversely, resuspension can be sought for cleaning of surfaces like solar photovoltaic panels (Du et al. 2019), equipment or production lines, or to prevent from cross-contamination between batches.

It is well established that the resuspension phenomenon is driven by the balance of forces experienced by particles. More precisely it occurs if the removal forces exceed the adhesive forces. For the simplest case of monolayer deposits excluding particle/particle interactions and considering only aerodynamic forces among the different removal forces, the force balance is thus driven by the particle/airflow interactions and the particle/wall surface interactions. These are the conditions addressed in this study. But even for this simplest case, the aerodynamic and adhesive forces are influenced by a lot of parameters related to the airflow, the duct wall surface and the particles. In order to study the effect of these parameters on the resuspension phenomenon, many experiments and models have been reported in the literature.

Most of these studies aim at predicting or measuring the fraction of particles detached or remaining on the duct wall versus mean airflow properties (free stream or near wall velocity, friction velocity). This enables depicting the intensity of the phenomenon that can be expected when exposing the deposit to an airflow exhibiting the given mean properties concerned. Many resuspension models dedicated to monolayer deposits have been developed, and have been summarized by Ziskind, Fichman, and Gutfinger (1995), Stempniewicz, Komen, and De With (2008), Zhang, Reeks, and Kissane (2013), Henry and Minier

(2014) and Nasr et al. (2019). As suggested by Henry and Minier (2014), they can be classified into empirical, static and dynamic models. Static models are based on force or momentum balances, to describe the disruption of the particle/surface static equilibrium. The formalism of these models is adapted to the main resuspension mechanism (which is generally assumed) among rolling, sliding or direct lifting. Some of these static models, like those of Reeks and Hall (2001) and Benito et al. (2018) take into consideration probability density functions (PDF) to represent the distribution of some parameters influencing the resuspension phenomenon. Dynamic models, like that of Guingo and Minier (2008) are based on the type of particle motion on the wall surface before detachment. Most of the aforementioned models lead to the calculation of the fraction of particles detached (or remaining on the duct wall) versus the friction velocity.

In parallel to these modeling works, many experimental studies were dedicated to the resuspension phenomenon for cases of monolayer deposits. Theron, Debba, and Le Coq (2020) summarized those conducted in wind tunnels, by emphasizing the experimental methodologies that were implemented; especially in terms of temporal airflow patterns to which particles were exposed; and the type of results that were reported. Most of these studies aimed at determining detachment fractions versus mean air velocity, free stream velocity or friction velocity, or threshold velocities responsible for the detachment of 50% of particles (Barth et al. 2014; Ibrahim, Dunn, and Brach 2003, 2004; Ibrahim, Dunn, and Qazi 2008; Ibrahim and Dunn 2006; Jiang et al. 2008). Depending on the experimental protocol employed, these detached fractions thus include particles resuspended over a longer or shorter time period, and airflow pattern backgrounds that can exhibit (transient) periods of acceleration.

The purpose of the present study is to describe how resuspension evolves over time for temporal airflow patterns mimicking situations of fan restart in HVAC systems, in order to depict the dynamic of the resuspension phenomenon, i.e., the evolution of its intensity over time. It is a typical case of transient airflow as it involves a period of air acceleration before reaching the targeted mean airflow velocity at steady state. Such time-resolved description of resuspension thus requires a particularly high acquisition frequency of fractions of particles detached or remaining on the duct wall. Except Kassab et al. (2013) who reported fractions of detached particles obtained at high acquisition frequency (of 2000 Hz), there are no other studies in the literature that addressed the dynamic of resuspension through such time-resolved approach. Braaten, Paw, and Shaw (1990), Ibrahim, Dunn, and Brach (2003), and Vincent et al. (2019) presented detached fractions versus time for temporal airflow patterns involving an acceleration period followed by steady state, but the acquisition frequencies were too low to have a fine description of the evolution of the phenomenon during the acceleration stage which is generally rather short.

Moreover, in the aim of focusing on real situations of fan restart, it is interesting to evaluate how the temporal evolution of the resuspension phenomenon is influenced by the properties of the temporal airflow pattern. When the acceleration is linear the properties of the temporal airflow pattern can be characterized by the mean acceleration and the mean velocity at steady state. Some studies (Braaten, Paw, and Shaw 1990; Kassab et al. 2013) evaluated the effect of the mean velocity at steady state on the fraction of particles remaining on the duct wall after a shorter or longer period. They showed that the remaining fraction is lower when the mean velocity at steady state increases.

The purpose of this study is to investigate by an experimental approach the influence of the temporal airflow pattern properties during the acceleration of a fan on the initiation of the resuspension phenomenon. To fulfill the expectations of presenting a time-resolved description of resuspension and to offer new perspectives for model developments, the experimental methodology involves the simultaneous recordings of the remaining fraction and the airflow characteristics. The airflow is characterized at a spatial scale relevant with the particle diameter, i.e., typically in the viscous sublayer (for microparticles of size ranging from several microns to several tens of micron).

2. Materials and methods

2.1. Temporal airflow patterns

The experimental facilities, materials and methods used to conduct the experiments are the same as those presented in Theron, Debba, and Le Coq (2020). The experimental methodology was detailed for one temporal airflow pattern (mean duct velocity at steady state of 7.6 $m.s^{-1}$ and mean acceleration of 2.1 $m.s^{-2}$). In the present study it is applied for nine new temporal airflow patterns in order to investigate the influence of the mean acceleration at steady state and the mean acceleration on the temporal evolution of the

Table 1. Experimental conditions tested (the aeraulic condition highlighted in italic is the one reported by Theron, Debba and Le Coq (2020)).

U_{mean} (m.s^{-1})	Re_h	α_{mean} (m.s^{-2})	Number of trials	T (°C)	RH (%)	C_0 (part.mm^{-2})
3.0	12,820	0.3	3	24	32	177 ± 56
		2.1	3	24	32	128 ± 45
5.0	21,370	0.3	5	21–24	30–35	115 ± 23
		2.1	5	20–24	30–35	135 ± 46
6.0	25,640	0.3	6	24	36–48	89 ± 10
		2.1	7	21–24	35–38	90 ± 35
7.6	32,480	0.3	7	21–24	21–38	132 ± 40
		2.1	*7*	*23–24*	*30–36*	*114 ± 17*
9.0	38,460	0.3	6	24–25	31–38	112 ± 30
		2.1	7	23–25	31–57	97 ± 20

fraction of particles remaining on the duct wall. In total, five mean velocities at steady state (from 3.0 to 9.0 m.s^{-1}) and two mean accelerations (0.3 and 2.1 m.s^{-2}) were tested (cf. Table 1). The ranges of these parameters have been selected in order to be relevant with those typically used in ventilation systems.

The conditions of the 56 resuspension experiments (several replicates were conducted for each temporal airflow pattern) that have been conducted are detailed in Table 1. U_{mean}, Re_h and α_{mean} are the mean duct velocity reached at steady state, the corresponding hydraulic Reynolds number and the mean acceleration, respectively. C_0 is the concentration of the initial deposit.

2.2. Experimental bench

The wind tunnel used to carry out experiments involves a test section of 2 m length and of 20×4 cm^2 rectangular cross section, which is made of antistatic PMMA. The measurement zone (at which the resuspension and velocity recordings were carried out), presented in Figure 1, is located at a distance from the entrance in the test section of $x = 1.3$ m, in order to be under established flow conditions.

2.3. Air velocity measurement

The velocity measurements were realized thanks to Hot Wire Anemometry (HWA) with a Dantec Constant Temperature Anemometry acquisition chain. For each experiment the air velocity was recorded simultaneously at two y distances from the duct wall: $y = 20$ mm (corresponding to the half duct height), and $y \approx 160$–430 µm (in the viscous sublayer) thanks to 55P11 and 55P15 probes, respectively. The probes were positioned at $z = 30$ mm from the vertical duct wall. The acquisition frequency was 1000 Hz.

2.4. Preliminary characterization of the viscous sublayer at steady state

Preliminary to resuspension experiments, vertical velocity profiles at steady state were sampled in order to determine the air friction velocity u^* and the viscous sublayer thickness δ. The friction velocity is obtained from the slope at origin of the velocity profile:

$$u^* = \sqrt{\nu . \frac{\partial u}{\partial y}_{y=0}} \quad (1)$$

where ν is the fluid kinematic viscosity.

This characterization was performed for $U_{mean} =$ 3.0; 5.0 and 7.6 m.s^{-1}. The u^* values obtained are given in Table 2. The following relationship between u^* and U_{mean} was determined, and was used to estimate the u^* values for $U_{mean} = 6.0$ and 9.0 m.s^{-1}:

$$u^* = 0.043.U_{mean} + 0.031 \quad (2)$$

The dimensionless vertical velocity profiles $u^+ = f(y^+)$ are presented in Figure 2. For $y^+ = 3$ to 8 (i.e., the y^+ range concerning the viscous sublayer), these profiles are in good agreement with profiles reported by Keirsbulck et al. (2012) and obtained by experimental measurements and DNS simulations, and allow determining the y^+ ranges corresponding to the different zones of the boundary layer: the logarithmic law involves y^+ values higher than 30 and the viscous sublayer corresponds to $y^+ = 0$–8. For each mean velocity the y value corresponding to $y^+ = 8$, i.e., the viscous sublayer thickness, is given in Table 2.

As reported in Theron, Debba, and Le Coq (2020) the HWA technique overestimates the velocity for y^+ values lower than 3 (corresponding to $y = 294$–135 µm for $U_{mean} = 3.0$–7.6 m.s^{-1}). This phenomenon is explained by a "near wall" conductive heat transfer effect in addition to the "free flow" convective heat transfer and to an increasing aerodynamic blockage effect due to the proximity of the wire and prongs to the wall (Hutchins and Choi 2002).

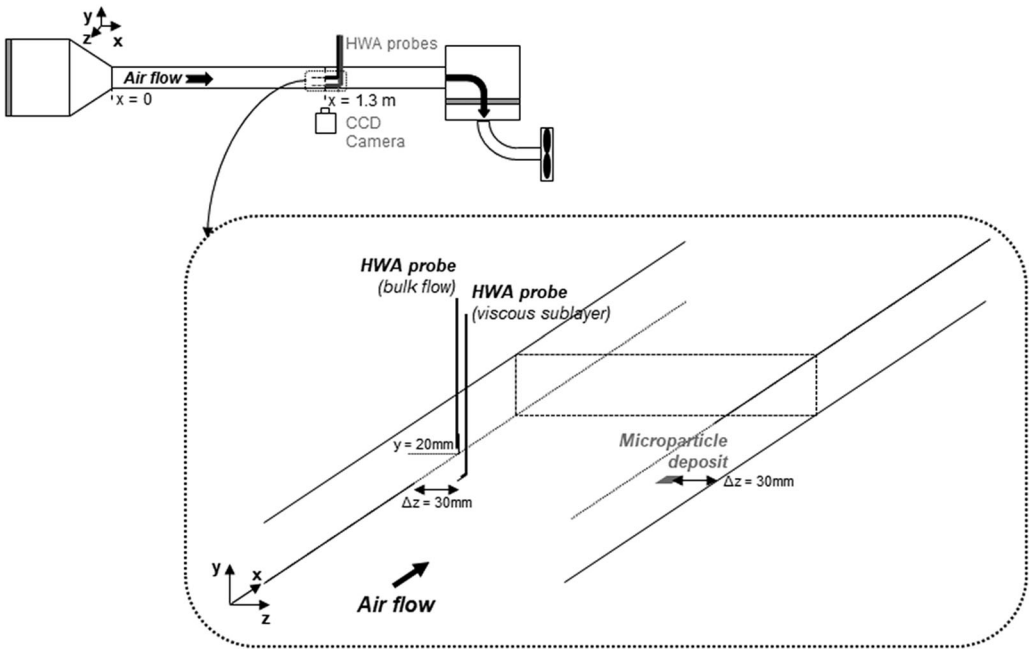

Figure 1. Diagram of the measurement zone of the experimental rig.

Table 2. Characteristics of the boundary layer for the mean velocities at steady state tested.

U_{mean} ($m.s^{-1}$)	δ (µm)	u* ($m.s^{-1}$)
3.0	770	0.16
5.0	510	0.25
6.0	–	0.29
7.6	*350*	*0.36*
9.0	–	0.42

2.5. Microparticles

The microparticles used to conduct resuspension experiments were spherical shaped bronze particles of 8000 $kg.m^{-3}$ density. Their size range was 3–30 µm, with a number size distribution characterized by a median diameter $D_{p,50}$ = 16 µm, and $D_{p,10}$ and $D_{p,90}$ values of 10 µm and 25 µm, respectively. The comparison of these values to δ values reported in Table 2 enables to ensure that particles are completely immersed in the viscous sublayer before reentrainment whatever the mean velocity at steady state.

2.6. Initial microparticle deposits

The experiments involved 1 cm^2 monolayer deposits for which the conditions of preparation were chosen in order to: i) achieve a statistically representative counting of particles in the field of view (2.0 × 1.5 mm^2); and ii) avoid as much as possible particle clusters to reduce particle/particle interactions. For each of the 10 temporal airflow patterns tested the mean concentration (in $part.mm^{-2}$) and standard deviation of the initial deposits are given in Table 1. The mean concentration of the initial deposit ranges from 89 to 177 $part.mm^{-2}$. Such values are quite high compared to concentrations reported in the literature, for example by Braaten (1994); Kassab et al. (2013), and especially Rondeau et al. (2021) who showed that for particle concentrations ranging from 35 to 100 $part.mm^{-2}$ a collision effect could be responsible for high resuspended fractions for particle size lower than 4.5 µm. For the present study, the films corresponding to several CCD camera recordings (for which the acquisition conditions are detailed below) were analyzed, and some collisions were observed. Based on these observations, it was estimated that the number of collisions per trial represents 1 to 9% of the initial number of particles of the deposit.

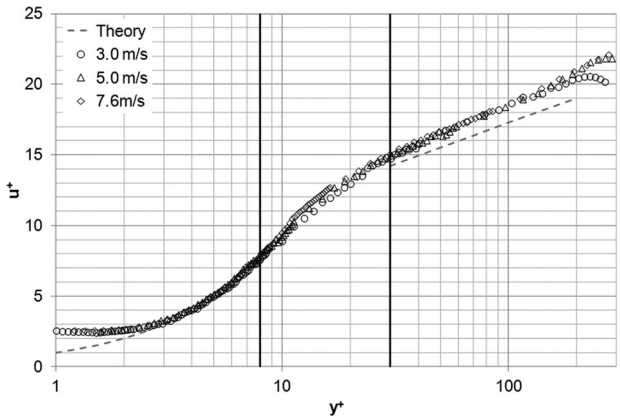

Figure 2. Dimensionless vertical velocity profiles at steady state for U_{mean} = 3.0; 5.0 and 7.6 $m.s^{-1}$.

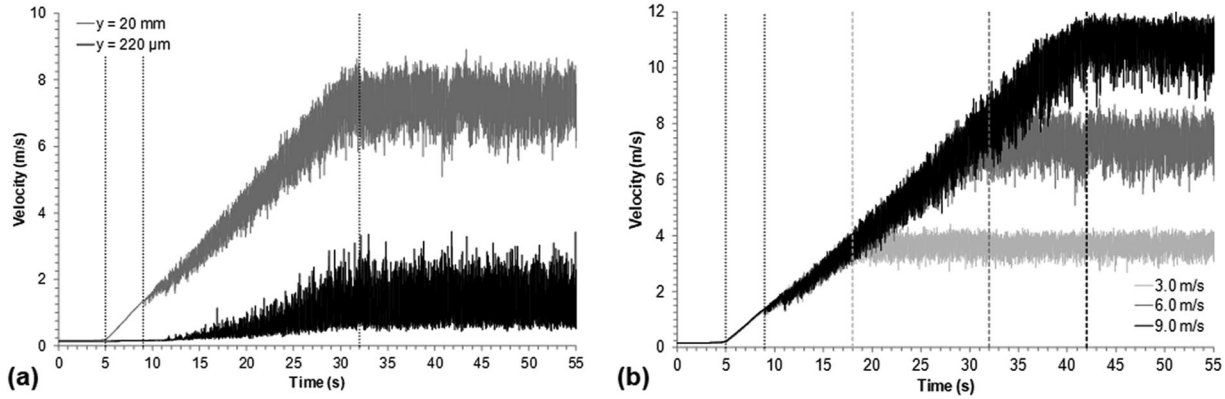

Figure 3. Temporal evolution of the velocity: (a) at the half duct height (y = 20 mm) and in the viscous sublayer ($y^+ = 4.1$, i.e., y = 220 µm) for $U_{mean} = 6.0\,m.s^{-1}$ and $\alpha_{mean} = 0.3\,m.s^{-2}$; (b) at the half duct height (y = 20 mm) for $U_{mean} = 3.0$; 6.0 and $9.0\,m.s^{-1}$ and $\alpha_{mean} = 0.3\,m.s^{-2}$.

2.7. Recording and treatment of images of particles remaining on the duct wall versus time

The number and size distribution of particles remaining on the duct wall as far as resuspension experiments occurred were characterized by an optical method. The field of view was located on the upstream side of the $1\,cm^2$ deposit in order to avoid newly resuspended particles emerging in pictures. A Speed Sense 1020 (Dantec Dynamics) CCD camera of 2320×1750 pixel^2 equipped with a zoom lens (La vision Lens) was used to achieve $2.0 \times 1.5\,mm^2$ pictures with a 1.2 µm/pixel resolution. The acquisition frequency was 45 Hz and 170 Hz for experiments involving mean accelerations of $0.3\,m.s^{-2}$ and $2.1\,m.s^{-2}$, respectively. In order to cover the acceleration period as well as a significant period of steady state the acquisition duration was set to 55 s and 14 s for the mean accelerations of $0.3\,m.s^{-2}$ and $2.1\,m.s^{-2}$, respectively.

For each temporal airflow pattern the curve representing the temporal evolution of the remaining fraction F was obtained thanks to the image processing methodology (using the Image J software) detailed in Theron, Debba, and Le Coq (2020). In this procedure particles of diameter lower than 9 µm are not counted. For experiments carried out at the mean acceleration of $0.3\,m.s^{-2}$ this methodology was applied to one out of three pictures over the whole number of recorded pictures, which resulted in a time step of 0.07 s between two treated pictures. For the mean acceleration of $2.1\,m.s^{-2}$ it was applied to one picture on ten, which resulted in a time step of 0.06 s between two treated pictures.

The evolution over time of the remaining fraction for the trial "i" of each temporal airflow pattern (as detailed in Table 1, 3 to 7 trials have been carried out for each temporal airflow pattern) is defined as follows:

$$F_i = 100.\frac{n_i(t)}{n_i(t=0)} \tag{3}$$

where $n_i(t)$ and $n_i(t=0)$ are the number of particles remaining on the duct wall in the field of observation at time t and the initial number of particles deposited on the duct wall for the trial "i", respectively.

To be more statistically representative (in terms of number of particles), for each temporal airflow pattern the temporal evolution of the remaining fraction F is calculated by taking into account the total number of trials:

$$\frac{F = 100.\sum_{i=1}^{nb\ \ trials} n_i(t)}{\sum_{i=1}^{nb\ \ trials} n_i(t=0)} \tag{4}$$

For temporal airflow patterns when resuspension occurred during every trials (see Section 3.2.2), $F = f(t)$ curves are fitted with a resuspension kinetic model corresponding to a decreasing exponential with a time delay as follows:

If $t < t^*$:

$$F_{fit}(t) = F_0 \tag{5}$$

If $t \geq t^*$:

$$F_{fit}(t) = F_{eq} + (F_0 - F_{eq}).e^{-\left(\frac{t-t^*}{\tau}\right)} \tag{6}$$

In Equations (5) and (6) F_0 and F_{eq} are the initial remaining fraction (100%) and the remaining fraction at the end of experiments (when stabilized), respectively. t^* and τ are the time at which resuspension starts and the time constant of the decreasing exponential, respectively. The F_{eq} value is determined by averaging the experimental remaining fraction at equilibrium: during the last 7 s and 2 s for the mean

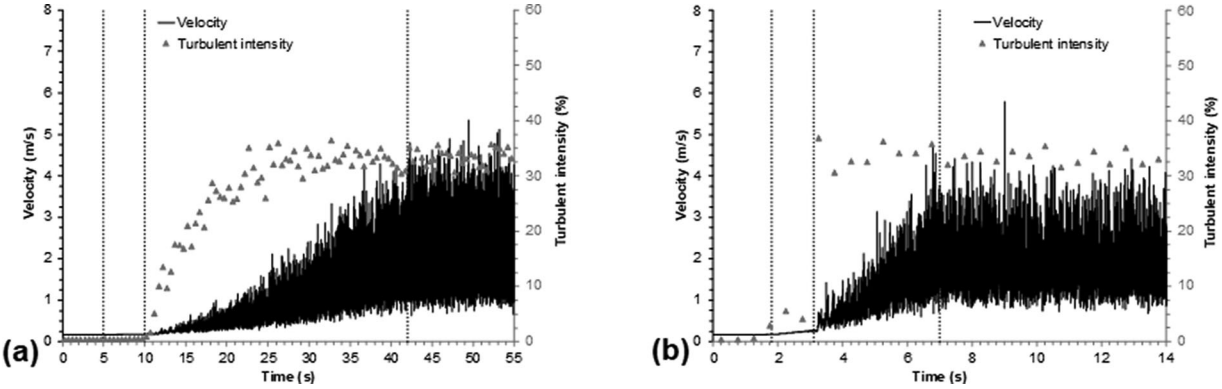

Figure 4. Temporal evolution of the velocity and the turbulent intensity in the viscous sublayer: (a) for $U_{mean} = 9.0\,m.s^{-1}$ and $\alpha_{mean} = 0.3\,m.s^{-2}$ (y = 180 µm); (b) for $U_{mean} = 9.0\,m.s^{-1}$ and $\alpha_{mean} = 2.1\,m.s^{-2}$ (y = 160 µm).

accelerations of $0.3\,m.s^{-2}$ and $2.1\,m.s^{-2}$, respectively. The t^* value is adjusted to fit with the experimental data.

3. Results and discussion

3.1. Characteristic times of the air velocity signal during the fan acceleration

Figure 3a represents the temporal evolutions of the velocity at the half duct height ($y = 20$ mm) and in the viscous sublayer ($y = 220$ µm, i.e., $y^+ = 4.1$) during the fan acceleration for the temporal airflow pattern involving $U_{mean} = 6.0\,m.s^{-1}$ and $\alpha_{mean} = 0.3\,m.s^{-2}$. As described in Theron, Debba, and Le Coq (2020), this graph shows that both velocity signals are synchronized. The velocity starts increasing 5 s after the fan start (beginning of the recording). The first fluctuations are observed at 9 s, even if they are less significant in the viscous sublayer. Steady state is reached at 32 s. Then velocities at the half duct height and in the viscous sublayer fluctuate around mean values of 7.5 and $1.2\,m.s^{-1}$, respectively. Similar conclusions can be drawn for the ten temporal airflow patterns tested. For each temporal airflow pattern both velocity signals were recorded three times, and a good reproducibility of the signals was obtained.

Figure 3b depicts the influence of U_{mean} on the velocity signal recorded at the half duct height for $\alpha_{mean} = 0.3\,m.s^{-2}$. Whatever the mean velocity to be reached at steady state the first two characteristic times of the velocity signal are similar: the delay between the fan start and the detection of the beginning of the velocity increase is 5 s, and the time required for the first fluctuations to appear is 9 s. The time at which steady state is reached increases with the targeted mean velocity. The conclusions are the same for the two other mean velocities tested for $\alpha_{mean} = 0.3\,m.s^{-2}$ as well as for the five mean velocities tested for $\alpha_{mean} = 2.1\,m.s^{-2}$. As expected the time at which steady state is reached is maximum for $U_{mean} = 9.0\,m.s^{-1}$ and is 42 and 11 s for the mean accelerations of 0.3 and $2.1\,m.s^{-2}$, respectively. Since for these accelerations the total recording times are 55 s and 14 s, this allows covering minimum steady state periods of 13 and 3 s, respectively.

The high frequency at which these signals were recorded (1000 Hz) enables some treatments of the raw velocity data to explore more deeply the temporal evolution of the air velocity properties, and especially in the viscous sublayer. In Figures 4a and b the temporal evolution of the velocity in the viscous sublayer is superimposed to the temporal evolution of the Turbulent Intensity for $U_{mean} = 9.0\,m.s^{-1}$. The turbulent intensity TI is calculated as follows:

$$TI = \frac{u'_{rms}}{\overline{u}} \tag{7}$$

where $\overline{u}$ and u'_{rms} are the mean components of the velocity and the root mean square fluctuating velocity, respectively. These two parameters are averaged from 500 velocity points which represent time steps of 0.5 s (calculations have been done using increasing number of data points from 100 points, and it was determined that 500 points was the minimum number of points required to obtain accurate values).

These two graphs show that whatever the mean acceleration, the Turbulent Intensity exhibits a similar evolution: it is 0 or relatively low during the acceleration phase without fluctuations, and significantly increases while fluctuations start (i.e., at t = 10 s and t = 3.1 s for $\alpha_{mean} = 0.3\,m.s^{-2}$ and $\alpha_{mean} = 2.1\,m.s^{-2}$, respectively). For both mean accelerations, a similar mean Turbulent Intensity between 30 to 35% is reached. This value seems to be reached almost immediately as soon as fluctuations start for the highest mean acceleration ($2.1\,m.s^{-2}$), whereas the Turbulent

Table 3. Remaining fractions at equilibrium obtained for the ten temporal airflow patterns tested.

U_{mean} (m.s^{-1})	Number of trials	α_{mean} (m.s^{-2})	$F_{eq,mean}$ (%)	σ (%)	$F_{eq,max}$ (%)	$F_{eq,min}$ (%)
3.0	3	0.3		*No resuspension*		
	3	2.1		*No resuspension*		
5.0	5	0.3		*No resuspension*		
	5	2.1	98	2	100	95
6.0	6	0.3	92	10	100	74
	7	2.1	97	3	100	92
7.6	7	0.3	86	7	98	78
	7	*2.1*	*79*	*5*	*85*	*70*
9.0	6	0.3	84	14	97	64
	7	2.1	82	7	95	74

Intensity increases progressively for the lowest tested mean acceleration (0.3 m.s^{-2}). For this last case, the mean stabilized Turbulent Intensity value is reached before steady state. Similar trends are obtained for the four other mean velocities at steady state.

For the ten temporal airflow patterns tested, the influence of the mean velocity at steady state and acceleration on the temporal evolution of the instantaneous velocity and turbulent intensity during the fan acceleration has been analyzed. In particular, it enabled to describe the four stages of the temporal airflow pattern to which the particles are exposed from the fan start up to steady state. The characteristic times corresponding to the transitions between these stages have been determined. It has been highlighted that these characteristic times are similar whatever the distance to the wall considered, from the bulk airflow up to the viscous sublayer. Thus, despite the fact that the HWA technique does not enable to record the velocity signal at wall distances of the order of magnitude of particle sizes, for each temporal airflow pattern the time at which the airflow switch from one stage to another one is known.

3.2. Evolution of the remaining fraction with time

3.2.1. Analysis of data representativeness

For each experiment, the film obtained thanks to the CCD camera recording enabled to determine whether or not resuspension had occurred. The phenomenon did not happen for all trials conducted at U_{mean} = 3.0 m.s^{-1} whatever the mean acceleration, as well as for trials carried out at U_{mean} = 5.0 m.s^{-1} and α_{mean} = 0.3 m.s^{-2}. For other temporal airflow patterns tested, in order to assess the representativeness of $F = f(t)$ curves three values of remaining fraction at equilibrium are given in Table 3: the $F_{eq,mean}$ value; calculated from the sum of all experiments; and $F_{eq,min}$ and $F_{eq,max}$ which correspond to the minimum and maximum F_{eq} values, respectively. These last two values are obtained by considering all trials separately.

The results reported in Table 3 show that rather significant deviations were observed between F_{eq} values obtained for the different trials carried out for each temporal airflow pattern. As mentioned by Theron, Debba, and Le Coq (2020) this is not explained by temperature and relative humidity variations, which are quite low (see Table 1), apart from experiments conducted at U_{mean} = 9.0 m.s^{-1} and α_{mean} = 2.1 m.s^{-2}. For these experiments, the RH range indicated in Table 1 is rather high: 31–57%, but among the seven trials five were performed for RH comprised between 31 and 35%, and only two at 57%. And among the seven trials no clear tendency was attributed to the relative humidity. Two possible assumptions can explain the rather significant deviations that were observed between F_{eq} values obtained for the different trials: the statistically low number of particles deposited for each trial, and the high initial particle concentration compared with the literature (Braaten 1994; Kassab et al. 2013; Rondeau et al. 2021) that could lead to some particle clusters. The counting representativeness issue raised by the first assumption could lead to variations of the mean adhesive force among deposits involved in each trial, and the counting uncertainty issue raised by the second assumption could lead to particle counting errors. Concerning this last point, for each trial the initial number of particles was counted manually and a maximum deviation of 14% compared to the value obtained by the image treatment procedure was accepted. Moreover, no clear tendency related to the initial deposit concentration C_0 was observed.

3.2.2. Influence of the temporal airflow pattern properties on the temporal evolution of the remaining fraction

The mean remaining fractions at equilibrium obtained for the ten temporal airflow patterns tested are presented in Table 3. Three possible scenarios were identified: (i) cases for which no resuspension occurred (U_{mean} = 3.0 m.s^{-1} whatever the mean acceleration and trials carried out at U_{mean} = 5.0 m.s^{-1} and α_{mean} = 0.3 m.s^{-2}) according to CCD camera recordings;

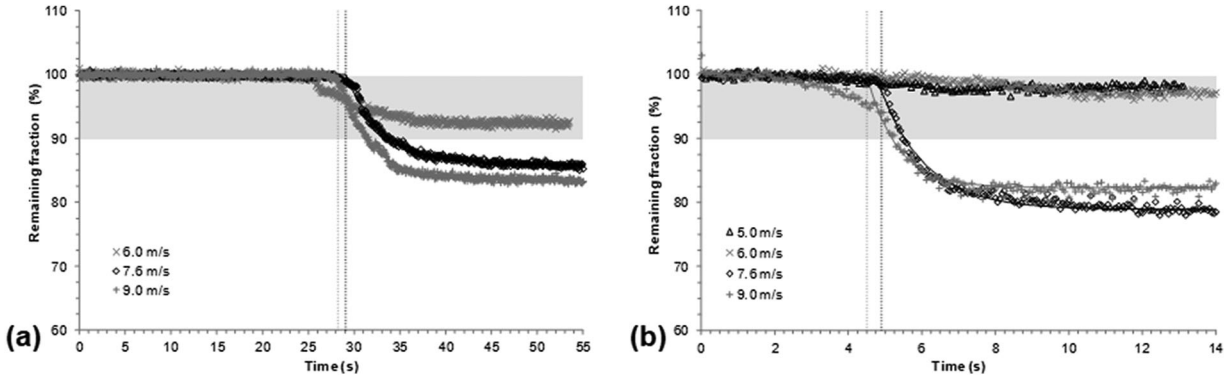

Figure 5. Temporal evolution of the remaining fraction: (a) for U_{mean} = 6.0; 7.6 and 9.0 m.s^{-1} and α_{mean} = 0.3 m.s^{-2}; (b) for U_{mean} = 5.0; 6.0; 7.6 and 9.0 m.s^{-1} and α_{mean} = 2.1 m.s^{-2}.

Table 4. Parameters of the mathematical model (see Equations (4) and (5)) fitted to the experimental temporal evolutions of the remaining fraction for the four temporal airflow patterns corresponding to the scenario (iii).

U_{mean} (m.s^{-1})	α_{mean} (m.s^{-2})	$F_{eq,mean}$ (%)	t* (s)	τ (s)
7.6	0.3	86	29.1	4.0
9.0		84	28.2	3.3
7.6	2.1	*79*	*4.8*	*1.1*
9.0		82	4.5	0.8

(ii) intermediate cases for which resuspension did not occur during every trials (trials carried out at U_{mean} = 5.0 m.s^{-1} and α_{mean} = 2.1 m.s^{-2}, and U_{mean} = 6.0 m.s^{-1} whatever the mean acceleration) and led to high $F_{eq,mean}$ values ranging from 92 to 98% as well as $F_{eq,max}$ = 100%; and (iii) cases for which resuspension occurred during every trials for the concerned temporal airflow pattern (U_{mean} = 7.6 and 9.0 m.s^{-1} whatever the mean acceleration) and led to $F_{eq,mean}$ values ranging from 79 to 86%.

Figure 5 presents the temporal evolutions of the remaining fraction corresponding to the seven temporal airflow patterns for which resuspension occurred. The vertical bars depict the time t^* at which resuspension starts (cf. Equation (4)) for temporal airflow patterns belonging to scenario (iii). The parameters of the resuspension kinetic model (Equations (4) and (5)) obtained for these last temporal airflow patterns are given in Table 4.

For the four temporal airflow patterns belonging to scenario (iii); i.e., experiments conducted at U_{mean} = 7.6 and 9.0 m.s^{-1} for both mean accelerations; the temporal evolutions of the remaining fraction exhibit similar shapes as that described in Theron, Debba, and Le Coq (2020) (for U_{mean} = 7.6 m.s^{-1} and α_{mean} = 2.1 m.s^{-2}). The values of characteristic times (t^* and τ) in Table 4; i.e., the parameters of the mathematical model that were fitted to the experimental data; suggest that these resuspension kinetic parameters are mostly driven by the mean acceleration. In fact for α_{mean} = 0.3 m.s^{-2} t^* is 28.2 and 29.1 s for U_{mean} = 9.0 and 7.6 m.s^{-1}, respectively, and for α_{mean} = 2.1 m.s^{-2} it is 4.5 and 4.8 s for U_{mean} = 9.0 and 7.6 m.s^{-1}, respectively. The τ values reported in Table 4 show that the resuspension kinetic is sharper for α_{mean} = 2.1 m.s^{-2}, as for this acceleration τ is approximately 1 s, while it is approximately 3–4 s for α_{mean} = 0.3 m.s^{-2}.

For these four temporal airflow patterns the remaining fractions at equilibrium are of same order of magnitude; between 79 and 86%. These values are rather high, but may be explained by the fact that the energy level of flow events are not high enough to exceed all the adhesive forces range exhibited by the studied particles/wall system. Due to the high number of parameters influencing the resuspension phenomenon it is difficult to compare directly the remaining fraction values reported by different authors. But despite this consideration it is interesting to notice that the aforementioned remaining fractions at equilibrium are quite close to those obtained by Kassab et al. (2013) for their experiments involving spherical glass particles of 10–30 µm deposited on a smooth substrate (made of glass, and with a mean surface roughness R_a = (0.536 ± 0.054).10^{-3} µm). In fact, they reported a detachment percentage of approximately 25% (corresponding to a remaining fraction of 75%) for deposits exposed to five seconds of airflow involving one second of acceleration and a mean velocity at steady state of 9 m.s^{-1}.

For the specific case of U_{mean} = 9.0 m.s^{-1} and α_{mean} = 2.1 m.s^{-2} the experimental data do not fit well with a decreasing exponential for the 3.0 to 4.7 s time period (see Figure 5b). In fact, the resuspension start that has been recorded experimentally is not as sharp as for other airflow conditions and the t^* value of 4.5 s determined from the kinetic model is higher than that estimated from the experimental curve

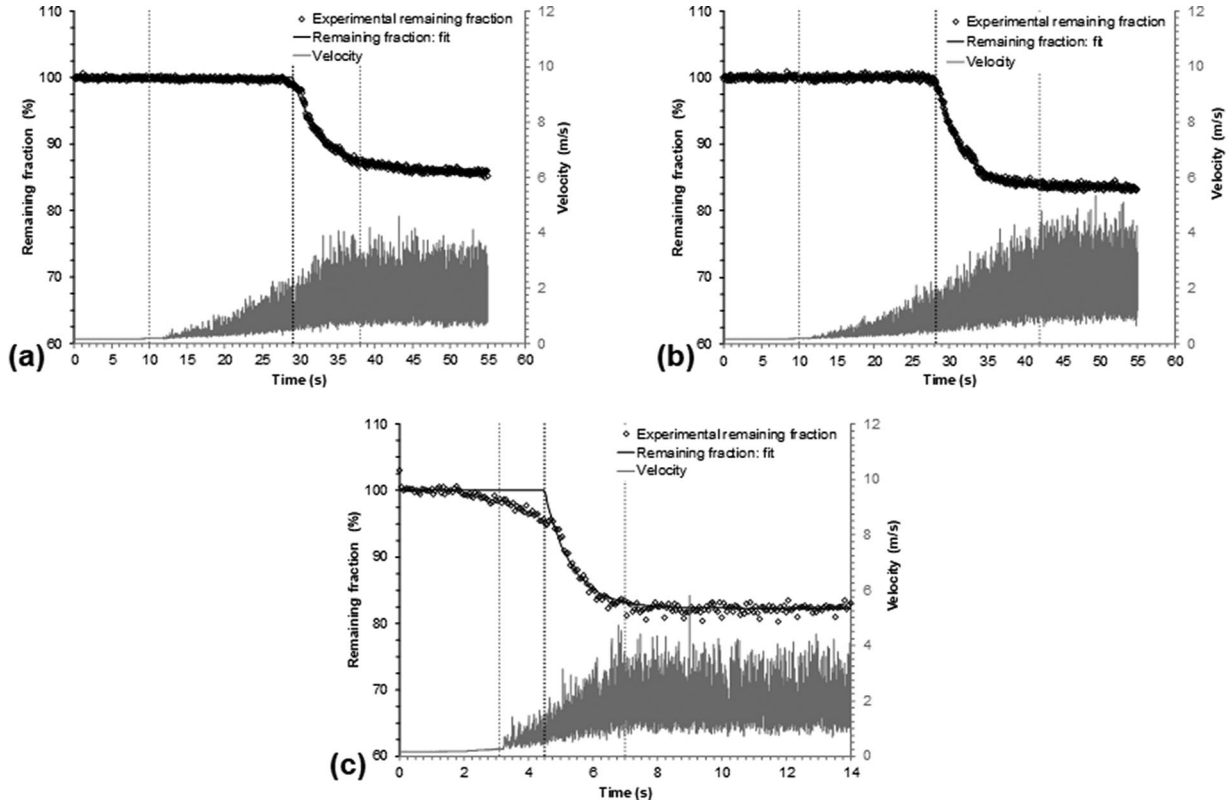

Figure 6. Temporal evolution of the remaining fraction versus temporal evolution of the velocity in the viscous sublayer: (a) for $U_{mean} = 7.6\,m.s^{-1}$ and $\alpha_{mean} = 0.3\,m.s^{-2}$ (y = 190 µm); (b) for $U_{mean} = 9.0\,m.s^{-1}$ and $\alpha_{mean} = 0.3\,m.s^{-2}$ (y = 180 µm); (c) for $U_{mean} = 9.0\,m.s^{-1}$ and $\alpha_{mean} = 2.1\,m.s^{-2}$ (y = 160 µm).

(approximately 3 s). For this temporal airflow pattern the same phenomenon has been observed for the seven reproducibility trials which have been realized. This may indicate that the "true" resuspension kinetic curve exhibits an inflexion point which is difficult to detect experimentally as it concerns the first instants of a very fast phenomenon, and a low range of remaining fraction values.

For experiments conducted at $U_{mean} = 5.0\,m.s^{-1}$ for $\alpha_{mean} = 2.1\,m.s^{-2}$ and $U_{mean} = 6.0\,m.s^{-1}$ for both accelerations the remaining fraction at equilibrium reached at steady state is very high: it ranges between 92 and 98%, and $F_{eq,max} = 100\%$. For these cases the number of particles concerned by resuspension is thus too low to interpret the characteristic times (t* and τ) of the resuspension kinetic.

3.3. Temporal evolution of the remaining fraction versus instantaneous wall velocity signal properties

3.3.1. Temporal evolution of the remaining fraction versus instantaneous velocity

In Figure 6 the temporal evolution of the remaining fraction is superimposed to the evolution of the velocity in the viscous sublayer for cases for which resuspension occurred during every trials, except for the case $U_{mean} = 7.6\,m.s^{-1}$ and $\alpha_{mean} = 2.1\,m.s^{-2}$ described in Theron, Debba, and Le Coq (2020). For the three temporal airflow patterns presented in this figure the graphs show that the resuspension phenomenon starts during the fan acceleration and more precisely during the acceleration with fluctuations stage. The onset of turbulence, i.e., the development of the first eddies, is thus not powerful enough to initiate the phenomenon.

Figure 6 also confirms, as mentioned by Braaten, Paw, and Shaw (1990), Kassab et al. (2013), and Vincent et al. (2019), that the temporal evolution of the remaining fraction is sharper during acceleration than at steady state. The remaining fraction keeps decreasing as steady state is reached but significantly more slowly. For experiments conducted at $U_{mean} = 9\,m.s^{-1}$ the equilibrium is almost reached at steady state (at 42 s for $\alpha_{mean} = 0.3\,m.s^{-2}$, Figure 6b, and at 7 s for $\alpha_{mean} = 2.1\,m.s^{-2}$, Figure 6c).

For the four temporal airflow patterns belonging to scenario (iii), the resuspension start corresponds to an average threshold velocity in the viscous sublayer ranging from 0.8 to $1.6\,m.s^{-1}$. As these values were not measured exactly at the same distance to the duct

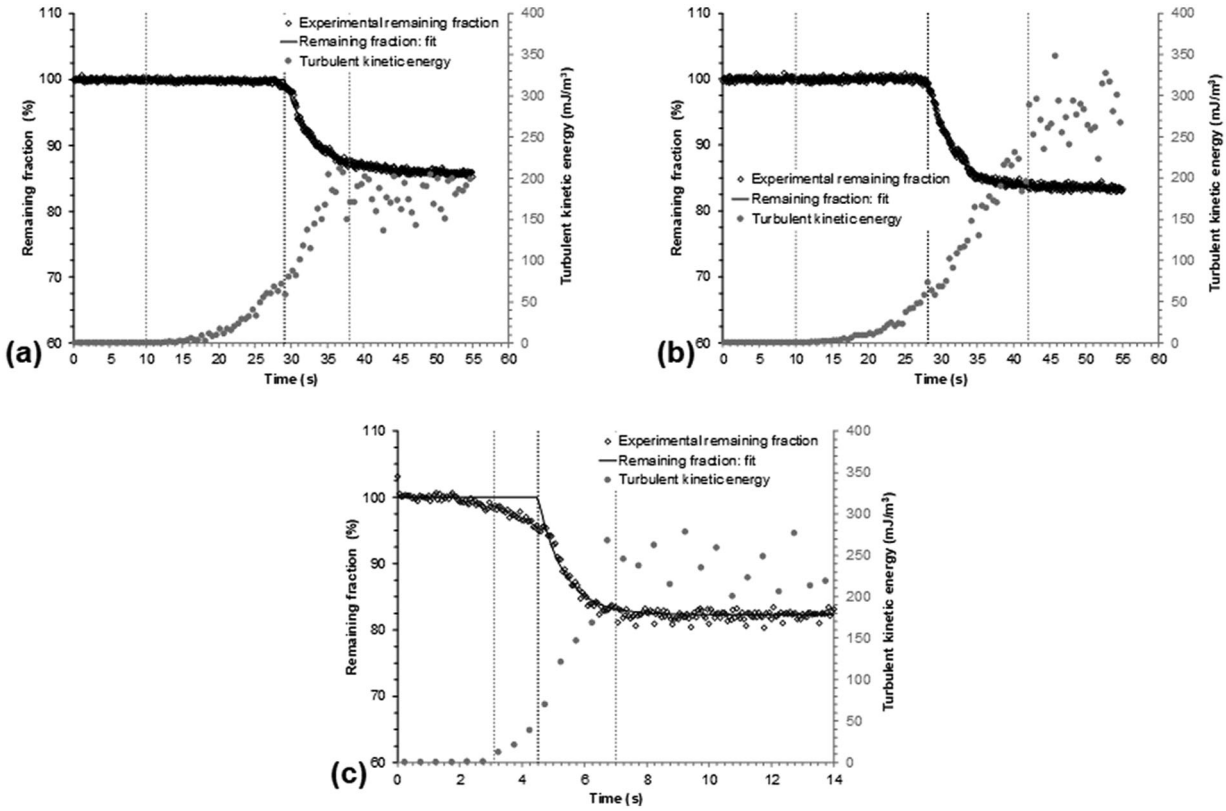

Figure 7. Temporal evolution of the remaining fraction versus temporal evolution of the Turbulent Kinetic Energy in the viscous sublayer: (a) for $U_{mean} = 7.6\,m.s^{-1}$ and $\alpha_{mean} = 0.3\,m.s^{-2}$ ($y = 190\,\mu m$); (b) for $U_{mean} = 9.0\,m.s^{-1}$ and $\alpha_{mean} = 0.3\,m.s^{-2}$ ($y = 180\,\mu m$); (c) for $U_{mean} = 9.0\,m.s^{-1}$ and $\alpha_{mean} = 2.1\,m.s^{-2}$ ($y = 160\,\mu m$).

wall ($y = 160$ to $290\,\mu m$ for the four airflow conditions), and at y values higher than the diameter of particles, it is difficult to interpret them quantitatively. For a more relevant comparison, the velocity measurements should be carried out deeper in the viscous sublayer (i.e., for lower y values), and at a similar y value for all the airflow conditions.

A unique threshold velocity, even measured at a duct wall distance relevant with particles diameter, cannot explain by itself the resuspension start value. In fact, the results described previously showed that the resuspension is initiated during the acceleration stage with velocity fluctuations which are characterized by their frequency and amplitude. Therefore, in the next section the temporal evolutions of the remaining fraction are analyzed regarding the temporal evolution of the turbulent kinetic energy, which involves both the mean and fluctuating components of the velocity.

3.3.2. Temporal evolution of the remaining fraction versus turbulent kinetic energy

The turbulent kinetic energy *TKE* in the viscous sublayer is calculated from the temporal evolution of the velocity in the viscous sublayer thanks to the following equation:

$$\mathrm{TKE} = \frac{1}{2}.\rho_{air}.\overline{u}^2.TI^2 \tag{8}$$

As for the calculation of the instantaneous turbulent intensity (Equation (7)), the turbulent kinetic energy is calculated from 500 velocity points, which corresponds to mean *TKE* values representing time steps of 0.5 s.

Figure 7 depicts the temporal evolution of the remaining fraction with that of the turbulent kinetic energy for the same temporal airflow patterns as those reported in Figure 6. This figure tends to confirm the assumption exposed in Theron, Debba, and Le Coq (2020) that a threshold *TKE* value is required to initiate the resuspension phenomenon. The threshold *TKE* ranges that have been determined for the four temporal airflow patterns considered are given in Table 5. In this table are also given the distances to the duct wall at which velocity signals were recorded in the viscous sublayer, noted y. Due to the fact that the y values reported in Table 5 are not strictly equal, the four threshold *TKE* ranges cannot be directly compared. Nevertheless both *TKE* ranges obtained for $\alpha_{mean} = 0.3\,m.s^{-2}$ and that estimated for $\alpha_{mean} = 2.1\,m.s^{-2}$ and $U_{mean} = 9.0\,m.s^{-1}$ are of the same order of

Table 5. Threshold TKE ranges determined for the four temporal airflow patterns corresponding to the scenario (iii).

U_{mean} (m.s^{-1})	α_{mean} (m.s^{-2})	y (µm)	$TKE_{threshold}$ (mJ/m^3)
7.6	0.3	190	70–80
9.0		180	57–67
7.6	2.1	*280*	*145–275*
9.0		160	38–70

magnitude as they involve y positions comprised in the rather small range of 160 to 190 µm. *TKE* intervals obtained for $\alpha_{mean} = 2.1\,m.s^{-2}$ are broader than those reported for $\alpha_{mean} = 0.3\,m.s^{-2}$. This comes from the fact that at $\alpha_{mean} = 2.1\,m.s^{-2}$ the velocity and as a consequence the *TI* increase faster than at $\alpha_{mean} = 0.3\,m.s^{-2}$; and thus the *TKE* as well. But as the time step between both *TKE* values is the same as for $\alpha_{mean} = 0.3\,m.s^{-2}$, the threshold *TKE* range cannot be determined with the same precision.

These considerations suggest that the initial slope of the resuspension kinetic is mostly driven by the instantaneous airflow properties, and thus by the mean acceleration. In fact, the threshold *TKE* value might probably depends on the adhesive force distribution of the particle/duct surface system, and especially the lowest value of this distribution. For a given mean acceleration, this *TKE* value will thus be exceeded at the same time whatever the mean velocity at steady state. The shape of detached fraction versus time curves obtained by Kassab et al. (2013) for glass beads initially deposited on a glass substrate may be explained by this hypothesis. Indeed, the temporal airflow patterns to which they exposed the particle deposit consisted in an acceleration of approximately 1 s followed by few seconds of steady state, for three different mean velocities at steady state (ranging from 9 to 16 m.s^{-1}). Deposits were thus exposed to increasing mean accelerations as velocity at steady state increased. And the time at which resuspension was initiated decreased for increasing mean velocity at steady state.

It can also be assumed that the remaining fraction reached at equilibrium depends on the mean velocity at steady state, with a decreasing tendency as the mean velocity at steady state increases. Such hypothesis cannot be strengthened by F_{eq} values reported in Table 4 for the temporal airflow patterns belonging to scenario (iii), as rather close remaining fractions at steady state are obtained for both U_{mean} tested. These two values might be not far enough to influence significantly the range of adhesive forces to be exceeded, and thus the amount of reentrained particles. But this hypothesis is supported by the results obtained by Kassab et al. (2013). Indeed, they reported increasing detachment percentages after a similar time of exposure to the airflow for increasing mean velocities at steady state. For example, for experiments involving 10-30 µm glass beads they reported mean detachment fractions ranging from approximately 25 to 53% for mean velocities at steady state ranging from 9 to 16 m.s^{-1}.

For experiments of the present study realized at $U_{mean} = 3.0\,m.s^{-1}$ (whatever the mean acceleration), it is highly probable that the threshold *TKE* value required to exceed even the lowest adhesive force associated with the particle/duct surface system has not been reached at all. For experiments conducted at $U_{mean} = 5.0\,m.s^{-1}$ it is possible that the *TKE* reached by the airflow was very close to the threshold value. This could explain why no resuspension was observed for $\alpha_{mean} = 0.3\,m.s^{-2}$ and that only few resuspension events were obtained for $\alpha_{mean} = 2.1\,m.s^{-2}$. For experiments carried out at $U_{mean} = 6.0\,m.s^{-1}$ the high F_{eq} values obtained may reflect the fact that the threshold *TKE* was slightly exceeded.

3.4. Temporal evolution of the resuspension rate

The resuspension rate, noted Λ, represents the instantaneous fraction of resuspended particles during the time step Δt. It is calculated as follows and is expressed in s^{-1}:

$$\Lambda = \frac{F(t) - F(t+\Delta t)}{\Delta t} \quad (9)$$

The resuspension rate is calculated at the same time step as the remaining fraction, i.e., at time steps of 0.07 and 0.06 s for experiments carried out at $\alpha_{mean} = 0.3\,m.s^{-2}$ and $\alpha_{mean} = 2.1\,m.s^{-2}$, respectively.

In Figure 8 the temporal evolution of the remaining fraction is superimposed to the temporal evolution of the resuspension rate for experiments conducted at $U_{mean} = 7.6\,m.s^{-1}$. Both graphs show that the resuspension rate exhibits fluctuations around 0 before the resuspension start. At t^* it starts increasing sharply, and reaches a maximum of approximately 7 s^{-1} (at 31 s) and 16 s^{-1} (at 5.5 s) for $\alpha_{mean} = 0.3\,m.s^{-2}$ and $\alpha_{mean} = 2.1\,m.s^{-2}$, respectively. It decreases until the remaining fraction reaches its equilibrium value, and then fluctuates around 0. Similar evolutions are obtained at $U_{mean} = 9.0\,m.s^{-1}$, with maximum Λ values of approximately 5 s^{-1} (at 30 s) and 12 s^{-1} (at 5.5 s) for $\alpha_{mean} = 0.3\,m.s^{-2}$ and $\alpha_{mean} = 2.1\,m.s^{-2}$, respectively. The rather significant fluctuations of Λ around 0 observed before t^* and after that the remaining fraction has reached its equilibrium are probably due to the fact that the image treatment

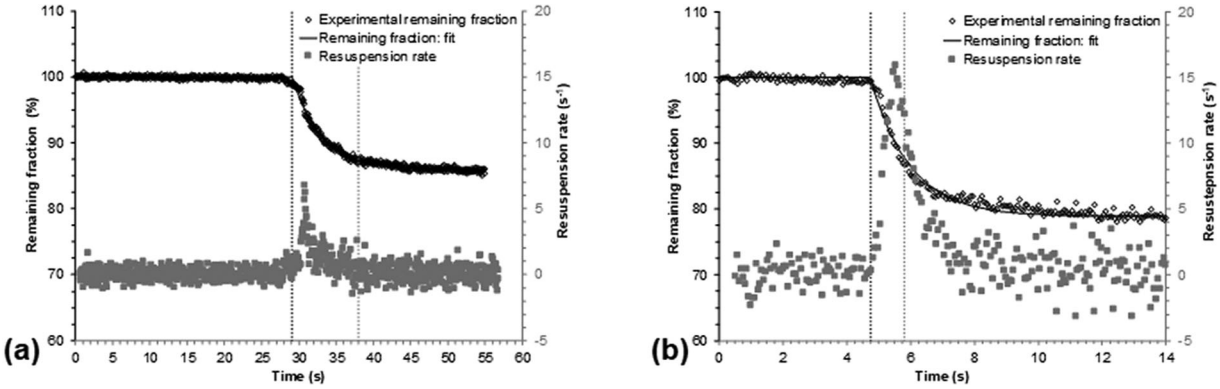

Figure 8. Temporal evolution of the remaining fraction versus temporal evolution of the resuspension rate for $U_{mean} = 7.6\,m.s^{-1}$: (a) for $\alpha_{mean} = 0.3\,m.s^{-2}$; (b) for $\alpha_{mean} = 2.1\,m.s^{-2}$.

procedure leads to remaining fraction values not strictly equal to 100%. For the six temporal airflow patterns belonging to scenarios (i) and (ii), the resuspension rate only fluctuates around 0 during the whole recording, and no peak is detected.

For particles representative of the 10–25 µm size range, these results enable to highlight that for cases for which resuspension happens the temporal evolution of the resuspension rate is mostly driven by the mean acceleration. In fact it affects the time at which the Λ peak appears (at 30 s and 5.5 s for $\alpha_{mean} = 0.3\,m.s^{-2}$ and $\alpha_{mean} = 2.1\,m.s^{-2}$, respectively), as well as the intensity of this peak. A slower mean acceleration leads to a Λ peak of lower intensity: 5-7 s^{-1} and 12-16 s^{-1} for $\alpha_{mean} = 0.3\,m.s^{-2}$ and $\alpha_{mean} = 2.1\,m.s^{-2}$, respectively. This can be explained by the fact that for a low acceleration the turbulent kinetic energy increases more progressively than for a high acceleration.

Very few studies of the literature reported experimental resuspension rate values for monolayer deposits, and more particularly temporal evolutions of instantaneous resuspension rate. Based on an experiment carried out with stainless steel microspheres of 70 µm diameter deposited on a glass surface and exposed to an accelerating velocity (to reach a free-stream velocity of $7\,m.s^{-1}$ at steady state in 11 s), Ibrahim, Dunn, and Brach (2003) plotted the detachment fraction versus time and estimated detachment rate values for both stages of the temporal airflow pattern. They obtained detachment rates of $4.6\,s^{-1}$ and $0.0075s^{-1}$ during the acceleration and the steady state stages, respectively. Due to the rather high time step they employed to represent their temporal evolution of the remaining fraction (of the order of magnitude of one point per second) these two resuspension rate values are averaged and thus do not allow for identifying some potential inflection point for each stage of the curve. From the temporal evolutions of the detached fraction obtained with glass particles deposited on different substrates, Kassab et al. (2013) calculated resuspension rates after a few seconds of steady state, and reported for example values ranging from approximately 0.03 to $0.3\,s^{-1}$ for a smooth substrate (glass). Vincent et al. (2019) estimated Λ values for the beginning of steady state, and obtained values of 6.10^{-5} to 6.10^{-4} s^{-1} for glass particles of diameter ranging from 5.6 to 22.8 µm.

For the present study it is not possible to give accurate resuspension rate values for the steady state stage due to the fluctuations that noise the experimental data (due to the fluctuations of the instantaneous remaining fraction data). The conclusion that can be made from the present results and the results reported by Kassab et al. (2013) and Vincent et al. (2019) is that the resuspension rate at steady state is far lower than during acceleration. In section 3.3.2 it is mentioned that the threshold *TKE* value required for the initiation of the resuspension phenomenon; which reflects the lowest values of the adhesive force distribution; is reached during the acceleration stage. It is possible that once the airflow is at steady state particles that are still on the duct wall; that exhibit higher adhesive forces than those which have been reentrained during acceleration; are removed by more energetic flow events that happen at random intervals. The low resuspension rate may thus be explained by the sudden and intermittent aspects of these events.

4. Conclusion

The temporal evolution of the fraction of particles remaining on the duct wall was studied for ten different temporal airflow patterns representative of a fan start (for mean velocity at steady state and mean acceleration ranges of 3.0–9.0 $m.s^{-1}$ and 0.3–2.1 $m.s^{-2}$,

respectively). The results led to classify the data into three scenarios: cases for which no resuspension happened, cases for which resuspension did not happen during each trials, and cases for which resuspension happened during each trials. For the most suitable temporal airflow patterns for resuspension to happen; i.e., for the highest tested mean velocities at steady state; it was shown that for the considered microparticles (representative of the 10–25 µm size range) and a rather smooth duct wall surface, a high fraction of particles (of the order of 80%) was still remaining on the duct wall after a few seconds of steady state.

The superimposition of the temporal evolution of the remaining fraction to the air velocity signal in the viscous sublayer enabled to demonstrate that when the resuspension phenomenon occurs, it starts during the acceleration with fluctuations stage of the velocity evolution. The high acquisition frequency at which the velocity signal was recorded thanks to Hot Wire Anemometry allowed for deriving the temporal evolution of the turbulent kinetic energy and to superimpose it to the temporal evolution of the remaining fraction. It was highlighted that the resuspension phenomenon might probably be initiated by a threshold turbulent kinetic energy value. These results also led to the conclusion that the shape of the resuspension kinetic is driven by the airflow pattern, i.e., by the mean acceleration, and that the remaining fraction at equilibrium depends on the mean velocity at steady state.

In order to better depict the instantaneous intensity of the resuspension phenomenon the temporal evolution of the resuspension rate, expressed in s^{-1}, was derived from the temporal evolution of the remaining fraction. This type of representation enabled to support the assumption that resuspension is more intense at its very beginning; during the acceleration stage of the velocity pattern; by quantitative values. And for high airflow accelerations the resuspension rates achieved are higher than for low accelerations. These results enable to strongly complement the literature that only report averaged resuspension rate values, generally calculated once steady state is reached.

The five mean velocities at steady state tested, even including cases for which no resuspension was observed, enable to broaden the experimental data available in the literature in terms of detachment fractions versus mean air friction velocity at steady state, which is important for the validation or development of mechanistic resuspension models. And the original time-resolved description of resuspension, including temporal evolutions of both instantaneous remaining fraction and air velocity in the viscous sublayer offers new modeling development perspectives.

Nomenclature

C_0	Concentration in particles of the initial deposit (part.mm^{-2})
D_p	Particle diameter (m)
F	Fraction of particles remaining on the duct wall (-)
F_{eq}	Fraction of particles remaining on the duct wall at equilibrium (-)
F_{mod}	Modeled fraction of particles remaining on the duct wall (-)
F_0	Fraction of particles remaining on the duct wall before resuspension start (-)
n_i	Number of particle remaining on the duct wall for the trial "i" (-)
RH	Relative humidity (-)
R_a	Mean surface roughness (m)
Re_h	Hydraulic Reynolds number at steady state (-)
t	Time (s)
t*	Time at which resuspension starts (s)
T	Temperature (°C)
TI	Turbulent intensity (-)
TKE	Turbulent kinetic energy (J.m^{-3})
u*	Friction velocity (m.s^{-1})
u'_{rms}	Root mean square of the turbulent velocity fluctuations (m.s^{-1})
$\overline{u}$	Mean velocity (m.s^{-1})
u^+	Dimensionless velocity (-)
x	Longitudinal distance to the entrance in the test section (m)
y	Vertical distance to the wall (m)
y^+	Dimensionless vertical distance to the wall (-)
z	Horizontal distance to the wall (m)
U_{fs}	Free stream velocity (m.s^{-1})
U_{mean}	Mean velocity at steady state (m.s^{-1})

Greek letters

α_{mean}	Mean acceleration (m.s^{-2})
δ	Viscous sublayer thickness (m)
Λ	Resuspension rate (s^{-1})
ρ_{air}	Air density (kg.m^{-3})
τ	Time constant of the resuspension kinetics (s)

Acknowledgments

The authors would like to acknowledge the Ecka Granules Company for supplying bronze particles.

Disclosure statement

The authors report there are no competing interests to declare.

References

Barth, T., J. Preuß, G. Müller, and U. Hampel. 2014. Single particle resuspension experiments in turbulent channel

flows. *J. Aerosol Sci.* 71:40–51. doi: 10.1016/j.jaerosci.2014.01.006.

Benito, J. G., R. O. Unac, A. M. Vidales, and I. Ippolito. 2018. Kinetic programmed resuspension – KPR technique. *J. Aerosol Sci.* 122:21–31. doi: 10.1016/j.jaerosci.2018.05.006.

Braaten, D. A., U. K. Paw, and R. H. Shaw. 1990. Particle resuspension in a turbulent boundary layer – observed and modeled. *J. Aerosol Sci.* 21 (5):613–28. doi: 10.1016/0021-8502(90)90117-G.

Braaten, D. A. 1994. Wind tunnel experiments of large particle reentrainment-deposition and development of large particle scaling parameters. *Aerosol Sci. Technol.* 21 (2):157–69. doi: 10.1080/02786829408959705.

Du, X., F. Jiang, E. Liu, C. Wu, and F. H. Ghorbel. 2019. Turbulent airflow dust particle removal from solar panel surface: analysis and experiment. *J. Aerosol Sci.* 130:32–44. doi: 10.1016/j.jaerosci.2019.01.005.

Guingo, M, and J. P. Minier. 2008. A new model for the simulation of particle resuspension by turbulent flows based on a stochastic description of wall roughness and adhesion forces. *Aerosol Sci.* 39 (11):957–73. doi: 10.1016/j.jaerosci.2008.06.007.

Henry, C, and J. P. Minier. 2014. Progress in particle resuspension from rough surfaces by turbulent flows. *Prog. Energy Comb. Sci.* 45:1–53. doi: 10.1016/j.pecs.2014.06.001.

Hutchins, N, and K. S. Choi. 2002. Accurate measurements of local skin friction coefficient using hot-wire anemometry. *Prog. Aerospace Sci.* 38 (4-5):421–46. doi: 10.1016/S0376-0421(02)00027-1.

Ibrahim, A. H., P. F. Dunn, and R. M. Brach. 2003. Microparticle detachment from surfaces exposed to turbulent air flow: controlled experiments and modeling. *Aerosol Sci.* 34 (6):765–82. 10.1016/S0021-8502(03)00031-4.

Ibrahim, A. H., P. F. Dunn, and R. M. Brach. 2004. Microparticle detachment from surfaces exposed to turbulent air flow: effects of flow and particle deposition characteristics. *Aerosol Sci.* 35 (7):805–21. doi: 10.1016/j.jaerosci.2004.01.002.

Ibrahim, A. H, and P. F. Dunn. 2006. Effects of temporal flow acceleration on the detachment of microparticles from surfaces. *Aerosol Sci.* 37 (10):1258–66. doi: 10.1016/j.jaerosci.2006.01.007.

Ibrahim, A. H., P. F. Dunn, and M. F. Qazi. 2008. Experiments and validation of a model for microparticle detachment from a surface by turbulent air flow. *Aerosol Sci.* 39 (8):645–56. doi: 10.1016/j.jaerosci.2008.03.006.

Jiang, Y., S. Matsusaka, H. Masuda, and Y. Qian. 2008. Characterizing the effect of substrate surface roughness on particle-wall interaction with the airflow method. *Powder Technol.* 186 (3):199–205. doi: 10.1016/j.powtec.2007.11.041.

Kassab, A. S., V. M. Ugaz, M. D. King, and Y. Hassan. 2013. High resolution study of micrometer particle detachment of different surfaces. *Sci. Technol.* 47 (4):351–60. doi: 10.1080/02786826.2012.752789.

Keirsbulck, L., G. Fourrié, L. Labraga, and M. Gad-el-Hak. 2012. Scaling of statistics in wall bounded turbulent flows. *C. R. Mecanique* 340 (6):420–33. doi: 10.1016/j.crme.2012.02.005.

Liu, Z., H. Niu, R. Rong, G. Cao, B. J. He, and Q. Deng. 2020. An experimental and numerical study of resuspension of fungal spore particles from HVAC ducts. *Sci. Total Environ.* 708:134742. doi: 10.1016/j.scitotenv.2019.134742.

Nasr, B., G. Ahmadi, A. R. Ferro, and S. Dhaniyala. 2019. Overview of mechanistic particle resuspension models: comparison with compilation of experimental data. *J. Adhes. Sci. Technol.* 33 (24):2631–60. doi: 10.1080/02786826.2019.1692126.

Reeks, M. W, and D. Hall. 2001. Kinetic models for particle resuspension in turbulent flows: theory and measurement. *Aerosol Sci.* 32 (1):1–31. doi: 10.1016/S0021-8502(00)00063-X.

Rondeau, A., S. Peillon, A. M. Vidales, J. Benito, R. Unac, J. C. Sabroux, and F. Gensdarmes. 2021. Evidence of inter-particles collision effect in airflow resuspension of poly-dispersed non-spherical tungsten particles in monolayer deposits. *J. Aerosol Sci.* 154:105735. doi: 10.1016/j.jaerosci.2020.105735.

Stempniewicz, M., E. Komen, and A. De With. 2008. Model of particle resuspension in turbulent flows. *Nucl. Eng. Des.* 238 (11):2943–59. doi: 10.1016/j.nucengdes.2007.11.024.

Theron, F., D. Debba, and L. Le Coq. 2020. Local experimental methodology for the study of microparticles resuspension in ventilated duct during fan acceleration. *J. Aerosol Sci.* 140:105477. doi: 10.1016/j.jaerosci.2019.105477.

Vincent, J. C., J. Hill, M. D. Walker, S. A. Smith, S. E. Smith, and N. E. Cant. 2019. Towards a predictive capability for the resuspension of particles through extension and experimental validation of the Biasi implementation of the "Rock'n Roll" model. *J. Aerosol Sci.* 137:105435. doi: 10.1016/j.jaerosci.2019.105435.

Zhang, F., M. Reeks, and M. Kissane. 2013. Particle resuspension in turbulent boundary layers and the influence of non-gaussian removal forces. *J. Aerosol Sci.* 58:103–28. doi: 10.1016/j.jaerosci.2012.11.009.

Ziskind, G., M. Fichman, and C. Gutfinger. 1995. Resuspension of particles from surfaces to turbulent flows – review and analysis. *J. Aerosol Sci.* 26 (4):613–44. doi: 10.1016/0021-8502(94)00139-P.